Electronic structure of $Au_{70}Pd_{30}$ disordered alloy

E. Arola and C. J. Barnes
Department of Physics, Tampere University of Technology, SF-33101 Tampere, Finland

R. S. Rao
Department of Physics, Tampere University of Technology, SF-33101 Tampere, Finland and National Physical Laboratory, Dr. K. S. Krishnan Road, New Delhi 110012, India

A. Bansil
Department of Physics, Northeastern University, Boston, Massachusetts 02115
(Received 6 March 1990)

We present angle-resolved photoemission (normal-emission) measurements from the (100) surface of a disordered $Au_{70}Pd_{30}$ alloy single crystal using He I, Ne I, He II, and Ne II excitations. The experimental results are interpreted via fully relativistic Korringa-Kohn-Rostoker coherent-potential-approximation computations of complex-energy bands, spectral densities, and total and site-decomposed densities of states in the alloy. Our measurements and calculations indicate that the main effects of adding Pd to Au are the following: (i) the appearance of a Pd-derived d-band complex with small dispersion, distinctly above the Au d-band edge, centered about 1 eV below the Fermi energy, (ii) the Au-derived d-band complex in the alloy is approximately 5 eV wide and is split by spin-orbit interaction into two peaks 2.1 eV apart, and (iii) levels of d symmetry generally suffer much larger disorder-induced smearings compared with those for levels possessing s-p symmetry.

I. INTRODUCTION

The *Au*Pd alloys form a continuous series of face-centered-cubic solid solutions over the entire composition range. A study of the electronic structure of these alloys is motivated not only by an intrinsic scientific interest, but also because this binary system possesses important catalytic properties.[1,2] Various experimental spectroscopies and techniques have been used to investigate chemisorption, surface segregation, diffusion, and reaction kinetics in these alloys.[3–7] A number of theoretical studies of the electronic structure of the *Au*Pd system, using a variety of computational methods, have also been reported in the literature.[8–10] Much of the existing experimental work on *Au*Pd has involved polycrystals. In this paper, we report the first angle-resolved photoemission measurements from the (100) face of a well-characterized substitutionally disordered single crystal of $Au_{70}Pd_{30}$ for several uv frequencies in order to help delineate characteristic effects of adding Pd on the electronic spectrum of Au. The experimental results are interpreted in terms of the corresponding relativistic Korringa-Kohn-Rostoker coherent-potential-approximation (KKR-CPA) electronic-structure computations.[11–14]

In particular, our measurements and calculations indicate that the addition of Pd to Au gives rise to a Pd-derived d-band complex with small dispersion centered about 1 eV below the Fermi energy, but distinctly above the Au-derived d bands in the alloy; this result differs from the earlier KKR-CPA calculations,[9] which suggest that the Pd-derived states mainly enter below the Au d-band edge in the alloy. The Au-derived d-band complex in the alloy is found to be approximately 5 eV wide and is split into two major peaks 2.1 eV apart by spin-orbit interaction. The disorder-induced smearing of bands in the alloy is strongly $\mathbf{k}$ and E dependent; states of s-p symmetry generally suffer much smaller dampings than those of d symmetry.

In this study we focus on comparing measured positions of various features in the angle-resolved spectra with corresponding complex-energy-band calculations, the latter playing the role of the familiar Bloch bands in a disordered alloy. Such an approach has been proven useful in delineating the electronic spectra of a number of transition- and noble-metal systems previously,[11,15] and as indicated above, in the present case of the *Au*Pd alloy. While further insight into the nature of the alloy spectrum should be possible via a direct calculation of the spectral intensities,[16] such a comparison is considered outside the scope of this work.

An outline of this paper is as follows. Section II summarizes general experimental and theoretical aspects, such as the details of sample preparation and characterization, and the construction of Au and Pd muffin-tin potentials used in the KKR-CPA computations. The angle-resolved spectra and the calculated complex-energy bands, spectral densities, and total and site-decomposed densities of states are presented and discussed in Sec. III. We comment also on the relevant experimental and theoretical literature pertaining to the electronic structure of *Au*Pd alloys. The Appendix gives an outline of a method for solving the KKR-CPA self-consistency equa-

tion; this method was found to yield solutions efficiently in *Au*Pd, even though other iterative procedures failed to converge at a number of energies.

II. EXPERIMENTAL AND THEORETICAL OVERVIEW

The experiments were performed using a multitechnique Vacuum Generators VG-ADES spectrometer, with *in situ* facilities for low-energy electron diffraction (LEED), Auger-electron spectroscopy (AES), angle-resolved photoemission spectroscopy (ARPES), and x-ray photoelectron spectroscopy (XPS) measurements. Ne I (16.85 eV), He I (21.22 eV), Ne II (26.90 eV), and He II (40.82 eV) unpolarized resonance lines from a gas discharge lamp were used to induce electron emission. ARPES spectra were recorded with an electrostatic analyzer operated at a constant pass energy of 5 eV, yielding a total instrumental resolution of ~ 100 meV.

The $Au_{70}Pd_{30}$ sample (Metal Crystals, Ltd., UK) oriented to within 0.5° of the {100} plane was in the form of a circular disk of diameter 4–5 mm and thickness order of 1 mm. After mechanical polishing the crystal was cleaned by a prolonged argon-ion bombardment (4 kV) while annealing at 700 K. A total of about 50 h of continual bombardment and annealing was carried out prior to carrying out ARPES measurements. After this treatment, the surface and bulk were free from contaminants as verified by XPS, AES, and the presence of sharp features in photoemission spectra with low background, expected for a well-crystallized, clean surface. The $Au_{70}Pd_{30}$(100) sample exhibited a $p(1\times1)$ LEED pattern. No indication of any surface reconstruction known to occur for a clean Au(100) surface,[17,18] was noted.[19] No superlattice or fractional order LEED spots were found, indicating that ordering on a range detectable by LEED does not occur.

In order to obtain a well-crystallized, *Au*Pd alloy surface for the accumulation of photoemission data, the sample was subjected to a brief (10 min) argon-ion bombardment while annealing at 700 K, and further annealed at 700 K for 10 min to remove the sputtering damage and equilibrate the surface. During the measuring periods the sample was "flashed" to 700 K every 1–2 h to desorb any chemisorbed species (CO,H_2), which slowly accumulate from the residual vacuum ($\sim 5\times10^{-11}$ Torr).

The surface segregation properties of the equilibrated alloy surface have been studied by AES, XPS, ion scattering spectroscopy, and carbon monoxide adsorption-desorption characteristics. The results indicate that the near-surface composition is similar to that of the bulk, in agreement with XPS results on cold-rolled *Au*Pd alloys.[5] The ion scattering measurements (ISS),[5] on the other hand, indicate that the first layer of the surface of the sputtered or heated samples is slightly enriched by Au throughout the composition range.

Concerning theoretical aspects, the present calculations employ the fully relativistic KKR-CPA scheme for treating disorder effects in a substitutional alloy.[11–14] The necessary Au and Pd muffin-tin potentials were constructed via the Mattheiss overlapping charge-density prescription, using $5d^{10}6s^1$ and $4d^{10}5s^0$ Libermann atomic charge densities for Au and Pd, respectively; full Slater exchange ($\alpha=1$) was employed. A fcc lattice of the observed lattice constant of $Au_{70}Pd_{30}$ ($a=7.592$ a.u.) was used in the overlapping procedure.

To help interpret our ARPES measurements, various physically relevant quantities were computed in $Au_{70}Pd_{30}$. These include complex-energy bands and spectral densities along the high-symmetry directions in the Brillouin zone, the total density of states, and the Au- and Pd-component densities of states. Our relativistic KKR-CPA formulation is similar to that of Ref. 12; we omit details for brevity.[20,21] It is noteworthy that, in solving the relativistic KKR-CPA self-consistency equation in *Au*Pd alloys, the simple iterative procedures as well as the method described in Ref. 11 failed to converge at many energies. An improved method for solving the KKR-CPA equation is outlined in the Appendix.

III. RESULTS AND DISCUSSION

Figure 1 presents He I, He II, Ne I, and Ne II excited normal-emission spectra from the (100) surface of the $Au_{70}Pd_{30}$ single crystal, together with the He I spectrum of Au(100).[22] The **k** values corresponding to various distinct features in the measured spectra were determined by assuming a free-electron final state.[23,24] Figure 2 compares the resulting experimental E-**k** points with the corresponding calculations along the $\Gamma-X$ direction. Figure 3 shows the total density of states decomposed into Pd and Au components as well as into the $d_{3/2}$ and $d_{5/2}$ contributions. Figure 4 displays a representative set of spectral density plots along the $\Gamma-X$ direction. We delineate changes in the electronic structure of Au induced by the addition of Pd with the help of Figs. 1–4.

Note first that, in contrast to Au in which the d-band edge lies at about 2 eV, $Au_{70}Pd_{30}$ yields strong emission in the range of 0 to 2 eV binding energies. In particular, the peak P_{Pd} is observed around -0.8 eV; this peak displays small dispersion, moving from 0.7 eV below the Fermi energy (E_F) for Ne I to 1.0 eV below E_F for He II or Ne II excitations [Fig. 2(a)].[25] These results are in good accord with our KKR-CPA calculations, which give a nearly dispersionless Pd-derived complex-energy band of Δ_7 symmetry in the alloy around -0.8 eV ending at Γ_{8^+}; the weak features at -2 eV in the Ne II and He II spectra appear to correlate with the second Pd-derived Δ_7 band terminating at Γ_{7^+}.[26] Figures 2(b) and 3 further show that the main structure in the Pd-component density in $Au_{70}Pd_{30}$ lies in the range 0 to 2 eV below E_F and is composed of states of $d_{3/2}$ and $d_{5/2}$ symmetry; most of the Pd-derived states are seen from Fig. 4 to suffer large (on the order of 1.5 eV, full width at half maximum) disorder broadenings.

For initial energies lower than -2 eV, changes in the spectra are less dramatic in that the Au and $Au_{70}Pd_{30}$ spectra qualitatively possess similar shapes [Fig. 1(a)]. The Au spectrum displays four distinct peaks, labeled $B-E$, a distinct shoulder A, and a slight shoulder F. Figure 2(c) shows that features C, D, and E are well correlated with the three lowest relativistic Au bands along line

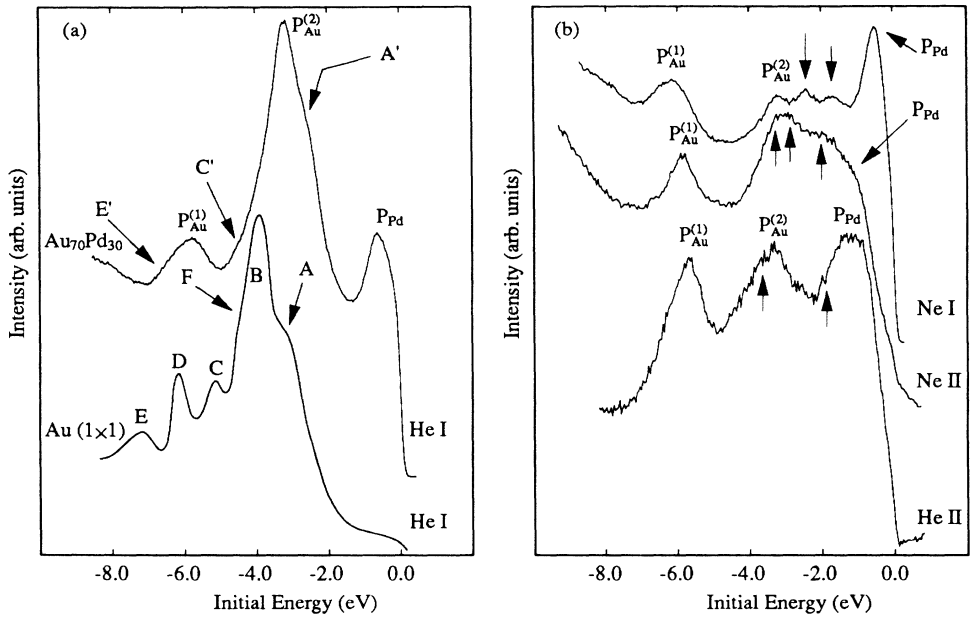

FIG. 1. Angle-resolved photoemission (normal emission) spectra from $Au_{70}Pd_{30}$(100) and Au(100) for different uv radiations. (a) He I spectrum from Au (Ref. 22) (lower) and $Au_{70}Pd_{30}$ (upper) and (b) He II, Ne II, and Ne I spectra from $Au_{70}Pd_{30}$. The angle of incidence of the light with respect to the surface normal is $\psi=45°$ for the alloy spectra; $\psi=40°$ for the Au spectrum. Various features indicated on the spectra are discussed in the text.

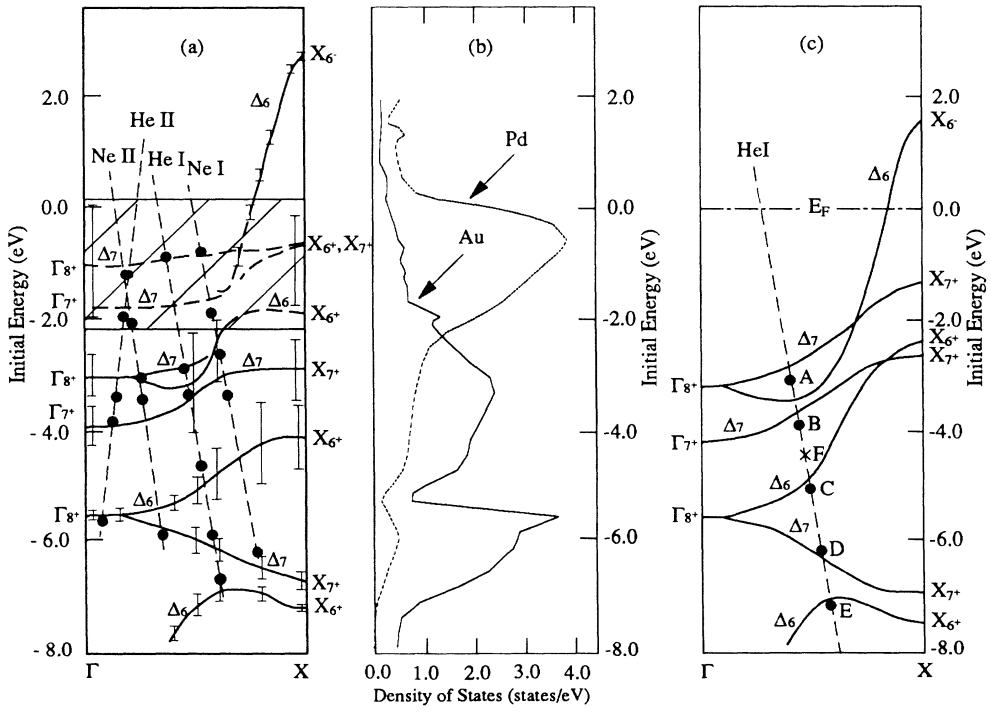

FIG. 2. (a) Relativistic KKR-CPA complex-energy bands in $Au_{70}Pd_{30}$ along the symmetry direction $\Gamma-X$. Typical disorder-induced smearings are shown by vertical bars around bands (the lengths of bars correspond to the full width at half maximum of the associated spectral peaks). Pd-derived d states suffer large disorder broadenings and are shown as a hatched band; all of the Pd-related bands (dashed) are not shown explicitly. Due to large smearings, the upper Au-related Δ_7 symmetric band is also not shown completely. Solid circles give the E-$\mathbf{k}$ points obtained from the spectra of Fig. 1; dashed lines connecting these circles depict the final state (free-electron) band for different radiations, rigidly shifted downwards by an amount equal to the photon energy (Ref. 24). (b) Pd and Au-component density of states in $Au_{70}Pd_{30}$. (c) Relativistic KKR bands in Au, along with the experimentally determined E-$\mathbf{k}$ values (solid circles, $A-E$, and the cross, F, discussed in the text) from the He I spectrum of Fig. 1(a). The energy zero in (a)–(c) is the Fermi energy.

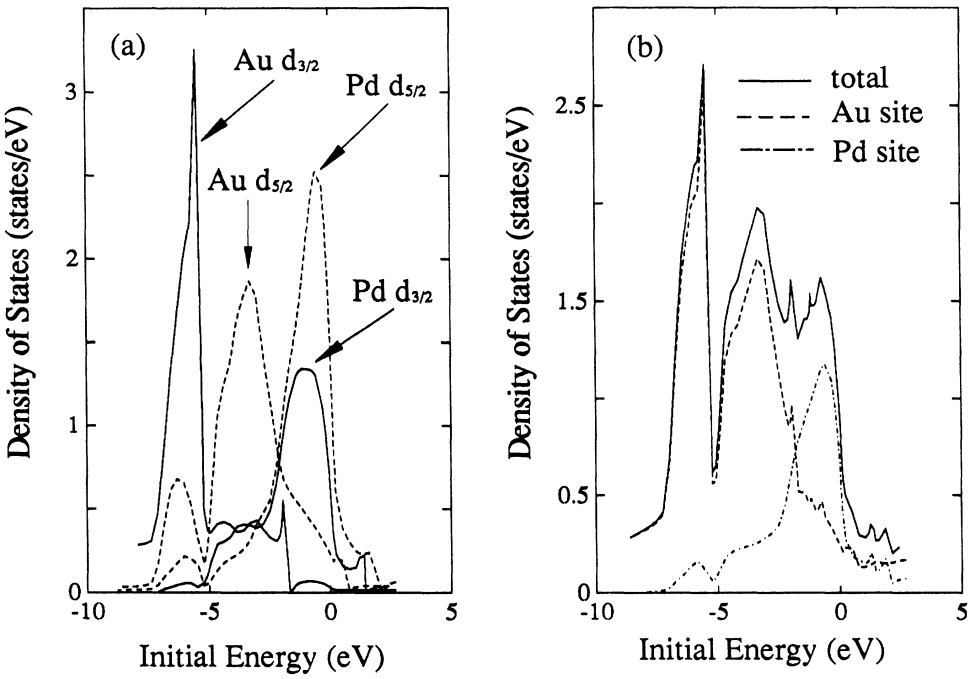

FIG. 3. Relativistic KKR-CPA densities of states in $Au_{70}Pd_{30}$. (a) Au and Pd component densities of states, decomposed into $d_{3/2}$ and $d_{5/2}$ channels; arrows identify various curves. (b) Total-density of states decomposed into contributions from Pd and Au sites. Energy zero denotes the Fermi energy.

$\Gamma-X$,[27,28] while A, B, and F appear to arise from the three uppermost bands; a more precise identification of the features $A-F$ would be interesting via synchrotron measurements using a continuous range of exciting frequencies.[29] Figure 2(a) nevertheless indicates a good overall accord between the calculated complex-energy bands and the positions of the various spectral features for four different radiations and allows us to reasonably delineate the electronic spectrum of the alloy.

The peaks D, E, and C, arising from the three lowest bands in Au [Fig. 2(c)], may be interpreted to give rise to the peak $P^{(1)}_{Au}$, the shoulder E', and the feature C', respectively, in the He I alloy spectrum [Fig. 1(a)]. The estimated energy positions of these features are in reasonable accord with the three lowest complex bands (symmetries Δ_6, Δ_7, and Δ_6) in $Au_{70}Pd_{30}$. All the relevant Au bands are considerably broadened upon alloying, so that only the peak D, which is the most prominent of the peaks C, D, and E, may be expected to remain distinct in the alloy. We further note that the theoretical dispersion of the lowest Δ_7 complex band is in good accord with the E-$\mathbf{k}$ values deduced for the peak $P^{(1)}_{Au}$ using different uv radiation [Fig. 1(b)]; features E' and C' were not analyzed in detail for the Ne I, Ne II, and He II alloy spectra, even though some similar features can be discerned in the measurements.

Concerning the remaining features B and A in the He I Au spectrum, Fig. 2(c) shows that these may be associated with the upper pair of Δ_7 bands.[29] In the $Au_{70}Pd_{30}$ He I spectrum, we see that the peak B moves to a lower binding energy but remains distinct ($P^{(2)}_{Au}$), and feature A yields a less pronounced shoulder A'. Here again there is a reasonable accord between the calculated complex alloy bands and the measured E-$\mathbf{k}$ values using different exciting frequencies [Fig. 2(a)]. The He II and Ne II spectra are generally of a poorer quality, due to the lower photon flux intercepting the sample and the identification of a number of weak features in these spectra as interband transitions is to be considered tentative.

We have measured additional He I and Ne I spectra (not shown) from the $Au_{70}Pd_{30}(100)$ surface for an incident light angle, $\psi=15°$, with the surface normal; the alloy spectra in Fig. 1 being for $\psi=45°$. As is well known, changes in the intensity of a spectral feature for different ψ values indicate the symmetry of the associated electronic state. For normal emission, with decreasing ψ, we expect emissions from d-type states to be enhanced, and from s-p type states to be reduced.[30] In the present case, when ψ is decreased from 45° to 15°, the features A' and E' become more prominent, while C' becomes less so, indicating that A' and E' are mostly d-type states, while C' contains a substantial s-p admixture. These observations are consistent with the specific initial states assigned above in the discussion of Fig. 2 to features $A-E$.

In view of the preceding theoretical and experimental results, the picture of the electronic structure of $Au_{70}Pd_{30}$ that emerges is that this is a split d-band system. The cross-hatched region in Fig. 2(a) between 0 and -2 eV is Pd derived; the Au-derived d bands extend roughly from -2 to -7 eV, and as seen from Fig. 2(b), consist of two main spin-orbit split portions lying about 2 eV apart. Thus, $Au_{70}Pd_{30}$ is rather like Cu-rich CuNi alloys,[31] with the Pd or Ni d states inducing an impurity virtual bound state roughly 1 eV below E_F in each case; also, the s-p

states in both alloys (e.g., Δ_6 band above E_F and below the d-band complex) behave in a virtual-crystal-like manner. The two alloys differ of course because relativistic effects in the host metal Cu are smaller than in Au. Interestingly, in Cu-rich *Cu*Pd,[32] Pd induces impurity bands above as well as below the host Cu d band.

The disorder-induced smearing of levels in $Au_{70}Pd_{30}$ shows a strong **k** and E dependence [Fig. 2(a)], as is common in transition- and noble-metal alloys.[14,15] Some representative values for the calculated smearings [shown by vertical bars around the complex bands of Fig. 2(a)] are as follows (in meV): Γ_{8^+} (lowest Au-like)=160; Γ_{7^+} (Au-like)=710; Γ_{8^+} (upper Au-like)=750; Γ_{8^+} (upper Pd-like)=2200; X_{6^+} (lowest Au-like)=120; X_{7^+} (lowest Au-like)=300; X_{6^+} (middle Au-like)=1200; X_{7^+} (middle Au-like)=1100; X_{6^+},X_{7^+} (the pair of levels at about -1.0 eV)=1600; and $X_{6^-}=140$. The s-p states [e.g., X_{6^+} (lowest), X_{6^-}] are thus seen to be much less broadened compared to d levels upon alloying, even though the broadening of d states varies widely among different bands.

We have considered the Fermi surface of $Au_{70}Pd_{30}$. Figure 5 compares the Fermi surface cross section in ΓXWK and $\Gamma XULK$ planes in Au and the alloy. Notably, our calculations predict the L-centered neck of Au to disappear in $Au_{70}Pd_{30}$. This is not surprising, because the L neck in Au is quite small, and the addition of an impurity (Pd) with a valence lower than Au would be expected to further reduce the neck size.

Finally, we comment briefly on other relevant experimental and theoretical work. On the experimental side, while we are not aware of any previous angle-resolved photoemission study of *Au*Pd single crystals, our results are consistent with earlier angle-integrated measurements on polycrystals; in particular, XPS spectra of Ref. 33 locate the Pd-induced virtual bound state at 1.55 eV and 1.4 eV binding energy, in $Au_{95}Pd_5$ and $Au_{90}Pd_{10}$, respectively. On the theoretical side, Ref. 8 considers a single Pd impurity in the Au matrix, and finds Pd-induced states above the Au d-band edge. CPA-based calculations (incorporated within a linear muffin-tin orbitals-type framework) of Ref. 10 in *Au*Pd alloys yield a density of states in qualitative accord with ours, especially with regard to the relative placement of the Au- and Pd-derived structures. However, Ref. 9, on the basis of their

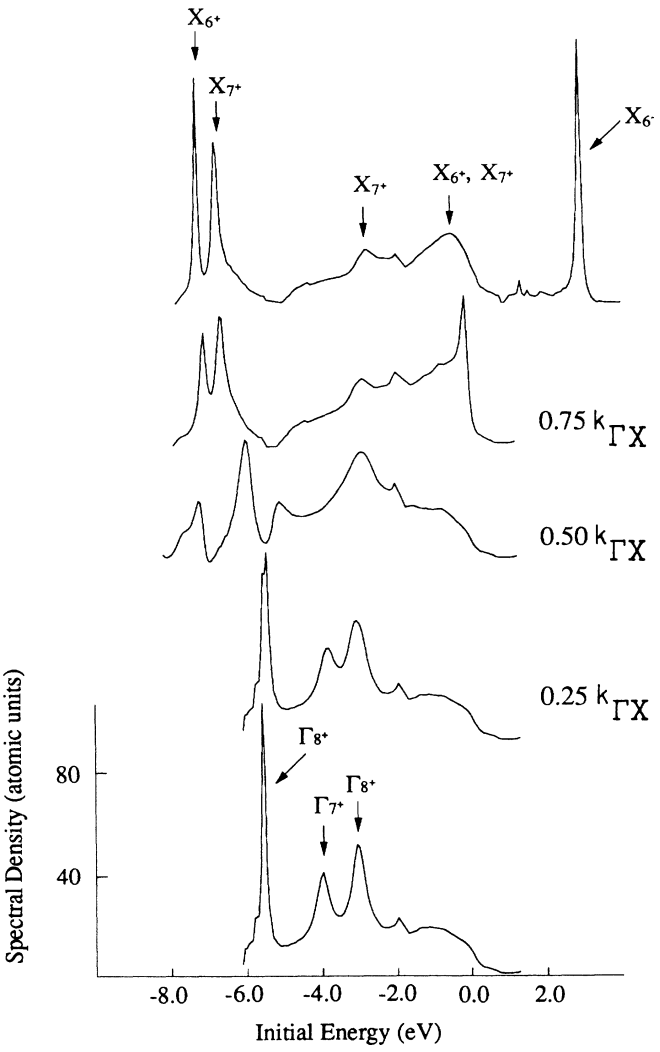

FIG. 4. The spectral density in $Au_{70}Pd_{30}$ for several k values along the symmetry direction Γ–X.

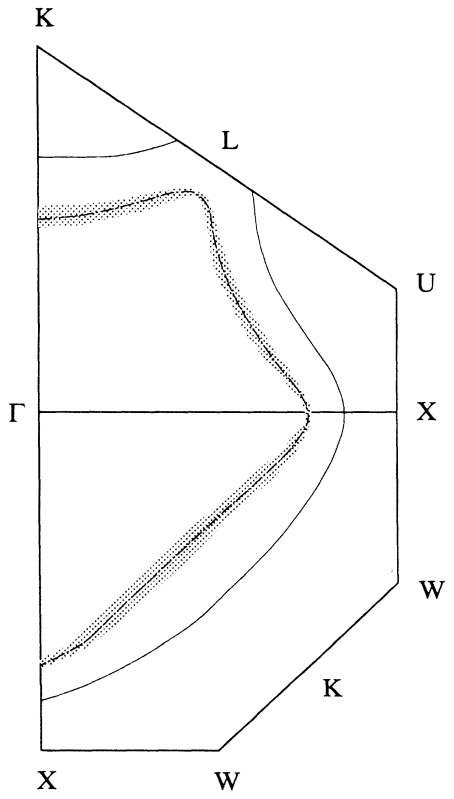

FIG. 5. The Fermi surface cross section in ΓXWK and $\Gamma XULK$ planes in Au (solid) and $Au_{70}Pd_{30}$ (shaded). The shading on the alloy curve represents the disorder smearing of the Fermi surface.

KKR-CPA computations, propose the electronic structure of *Au*Pd alloys to be such that the Pd-induced states lie below the Au *d*-band edge; this result differs from the theoretical model presented here, and is not consistent with the present and previous photoemission measurements. The differences in the present computations and those of Ref. 9 arise presumably from the use of different Au and Pd muffin-tin potentials.

ACKNOWLEDGMENTS

We are grateful to Professor M. Pessa for support and encouragement. Discussions with Dr. M. Lindroos are acknowledged. This project was supported by U.S. Department of Energy Grant No. ER45223, and a travel grant under the U.S./Finland program of the U.S. National Science Foundation (NSF), and benefited from the allocation of supercomputer time on the Cray Research, Inc. ER-Cray supercomputer of the National Energy Research Supercomputer Center at Lawrence Livermore National Laboratory (LLNL) and the San Diego Supercomputer Center. Acknowledgment is made to the donors of The Petroleum Research Fund, administered by the American Chemical Society (ACS), for partial support of this research. One of us (E.A.) is indebted to Tampere Research Foundation and to Finnish Science Academy for research grants. Another (C.J.B.) acknowledges Neste Foundation for financial support.

APPENDIX: AN IMPROVED METHOD FOR SOLVING THE KKR-CPA EQUATION

We start with the KKR-CPA condition in the form[34]

$$x[(\tau_{\rm CP}^{-1}-\tau_A^{-1})^{-1}-T_{00}^{\rm CP}]^{-1}+(1-x)[(\tau_{\rm CP}^{-1}-\tau_B^{-1})^{-1}-T_{00}^{\rm CP}]^{-1}=0\ , \tag{A1}$$

where much of the notation is obvious. Equation (1) has the advantage that it explicitly possesses the full double-point-group symmetry of the cubic lattice.

Following along the steps of Ref. 11, we rewrite Eq. (1) as $\mathbf{x}=\mathbf{f}(\mathbf{x})$ (here $\mathbf{x}$ denotes the vector of linearly independent elements of $\tau_{\rm CP}^{-1}$); a multidimensional Newton-Raphson formula for solving the KKR-CPA equation is then obtained straightforwardly, where the Jacobian matrix $\partial f_l/\partial x_m$ is

$$\begin{aligned}\frac{\partial f_l}{\partial x_m}=&(I_m)_{K(l)L(l)}-x\Bigg[[(\tau_{\rm CP}^{-1}-\tau_A^{-1})^{-1}-T_{00}]^{-1}\Bigg[N^{-1}\sum_{\mathbf{k}}(\tau_{\rm CP}^{-1}-B_{\mathbf{k}})^{-1}I_m(\tau_{\rm CP}^{-1}-B_{\mathbf{k}})^{-1}-(\tau_{\rm CP}^{-1}-\tau_A^{-1})^{-1}I_m(\tau_{\rm CP}^{-1}-\tau_A^{-1})^{-1}\Bigg]\\&\times[(\tau_{\rm CP}^{-1}-\tau_A^{-1})^{-1}-T_{00}]^{-1}\Bigg]_{K(l)L(l)}\\&-(1-x)\Bigg[[(\tau_{\rm CP}^{-1}-\tau_B^{-1})^{-1}-T_{00}]^{-1}\Bigg[(1/N)\sum_{\mathbf{k}}(\tau_{\rm CP}^{-1}-B_{\mathbf{k}})^{-1}I_m(\tau_{\rm CP}^{-1}-B_{\mathbf{k}})^{-1}\\&-(\tau_{\rm CP}^{-1}-\tau_B^{-1})^{-1}I_m(\tau_{\rm CP}^{-1}-\tau_B^{-1})^{-1}\Bigg][(\tau_{\rm CP}^{-1}-\tau_B^{-1})^{-1}-T_{00}]^{-1}\Bigg]_{K(l)L(l)}\ .\end{aligned} \tag{A2}$$

Here, $K(l)$ and $L(l)$ are the matrix indices corresponding to the lth element in $\mathbf{x}$ vector, $B_{\mathbf{k}}$ is the relativistic structure matrix, and the matrix $I_m\equiv\partial\tau_{\rm CP}^{-1}/\partial x_m$. Starting from the average-t-matrix values, the iterative procedure based on Eqs. (1) and (2) was found to converge efficiently at all energies in the present calculations.

[1]E. G. Allison and G. C. Bond, Catalysis Rev. **7**, 233 (1972).
[2]R. L. Moss and L. Whalley, in *Advances in Catalysis*, edited by D. D. Eley, H. Pines, and P. B. Weisz (Academic, New York, 1972), p. 158.
[3]A. Jablonski, S. H. Overbury, and G. A. Somorjai, Surf. Sci. **65**, 578 (1977); G. Betz, J. Dudonis, and P. Braun, *ibid.* **104**, L185 (1981).
[4]G. Maire, L. Hilaire, P. Legare, F. G. Gault, and A. O'Cinneide, J. Catal. **44**, 293 (1976).
[5]P. Varga and G. Hetzendorf, Surf. Sci. **162**, 544 (1985); G. Hetzendorf and P. Varga, Nucl. Instrum. Methods Phys. Res. Sect. B **18**, 501 (1987).
[6]D. G. Swartzfager, S. B. Ziemecki, and M. J. Kelley, J. Vac. Sci. Technol. **19**, 185 (1981).
[7]D. D. Eley, J. Res. Inst. Catal., Hokkaido Univ. **16**, 101 (1968).
[8]M. G. Ramsey and P. V. Smith, J. Phys. F **12**, 1697 (1982).
[9]H. Müller, H. Kirchmayr, P. Weinberger, P. Marksteiner, and J. Redinger, Z. Phys. B **67**, 193 (1987); P. Weinberger, R. Dirl, A. M. Boring, A. Gonis, and A. J. Freeman, Phys. Rev. B **37**, 1383 (1988).
[10]J. Kudrnovský and V. Drchal, Phys. Status Solidi B **148**, K23 (1988); J. Kudrnovský and J. Mašek, Phys. Rev. B **31**, 6424 (1985); J. Kudrnovský, V. Drchal, and J. Mašek, *ibid.* **35**, 2487 (1987).
[11]E. Arola, R. S. Rao, A. Salokatve, and A. Bansil, Phys. Rev. B **41**, 7361 (1990).
[12]J. Staunton, B. L. Gyorffy, and P. Weinberger, J. Phys. F **10**, 2665 (1980); P. Weinberger, J. Staunton, and B. L. Gyorffy, *ibid.* **12**, 2229 (1982).
[13]H. Ehrenreich and L. Schwartz, in *Solid State Physics*, edited

by H. Ehrenreich, F. Seitz, and D. Turnbull (Academic, New York, 1976), Vol. 31.

[14]For a recent review, see A. Bansil, in *Electronic Band Structure and its Applications,* edited by M. Yussouff (Springer-Verlag, Berlin, 1987), p. 273.

[15]H. Asonen, M. Lindroos, M. Pessa, R. Prasad, R. S. Rao, and A. Bansil, Phys. Rev. B **25**, 7075 (1982); A. Bansil, R. S. Rao, R. Prasad, H. Asonen, and M. Pessa, J. Phys. F **14**, 273 (1984); R. S. Rao, A. Bansil, H. Asonen, and M. Pessa, Phys. Rev. B **29**, 1713 (1984); R. S. Rao and M. Pessa, in *Electronic Band Structure and its Applications,* edited by M. Yussouff (Springer-Verlag, Berlin, 1987).

[16]G. M. Stocks and H. Winter, in *The Electronic Structure of Complex Systems,* edited by P. Phariseau and W. M. Temmerman (Plenum, New York, 1984). See also article by P. J. Durham in this volume.

[17]H.-G. Zimmer and A. Goldmann, Surf. Sci. **176**, 115 (1986).

[18]P. Heimann, J. Hermanson, H. Miosga, and H. Neddermeyer, Phys. Rev. Lett. **43**, 1757 (1979).

[19]Interestingly, the Au(100) (5×20) reconstructed surface possesses surface-state resonances, observable in normal emission, while the (1×1) Au(100) surface does not (Ref. 17). Consistent with our LEED observation of a $p(1\times1)$ alloy surface, no indication of such surface states in $Au_{70}Pd_{30}$ was seen in the present measurements.

[20]Some details are outlined in Ref. 11. For an extensive discussion of the formalism, see Ref. 21. Much of the present work utilizes real space Green's-function based formulas. As in the case of *Cu*Au, little difference was found between densities of states (total and component) computed via Lloyd formulas (Refs. 13 and 21) and Green's function based (Ref. 12) approaches.

[21]E. Arola, Ph.D. thesis, Tampere University of Technology, 1990.

[22]The Au(100) spectrum in Fig. 1(a) is reproduced from Ref. 17.

[23]If a free-electron final-state band is assumed, the final state **k** vector can be written as, $|\mathbf{k}^f|=[(2m^*)^{1/2}/\hbar](E_K-V_0)^{1/2}$, where m^* is the effective mass of the electron in the final state, V_0 is the "inner potential" or the bottom of the free-electron parabola with respect to the vacuum level, and E_K is the kinetic energy of the electron outside the crystal. Also, $E_K=\hbar\omega+E_i-\phi$, where $\hbar\omega$ is the photon energy, E_i the initial-state energy with respect to the Fermi level, and ϕ is the work function. The **k** values in $Au_{70}Pd_{30}$ in this work were determined by using effective-mass and inner-potential values for Au, which are $m^*=1.16m_e$ and $V_0=-7.11$ eV. These values were obtained by fitting the free-electron final-state **k**-vector formula for the experimental final-state **k** vectors found by means of the triangulation method for Au(111) and Au(110) spectra of R. Courths, H. Wern, U. Hau, B. Cord, V. Bachelier, and S. Hüfner, J. Phys. F **14**, 1559 (1984). The corresponding values for Pd, obtained from the data of F. J. Himpsel and D. E. Eastman [Phys. Rev. B **18**, 5236 (1978)], are $m^*_{Pd}=1.00m_e$ and $V_0^{Pd}=-7.7$ eV. Given the similarity of the free-electron parameters for Au and Pd, and the fact that we are studying a Au-rich *Au*Pd alloy, our use of the Au parameters in determining the E-**k** values is justified.

[24]The He II final-state line (dashed) in Fig. 2(a) possesses an opposite tilt to others because the final-state branch of the free-electron parabola for He II turns out to be different from the lower frequency Ne I, Ne II, and He I radiations.

[25]In connection with the Ne II spectra, it should be noted that the Ne II radiation from a resonance lamp is contaminated by a satellite line at 0.9 eV higher photon energy compared to the main line at 26.90 eV.

[26]We emphasize that the Pd-derived d bands suffer large disorder smearings, and not all of the associated bands (dashed) are shown explicitly in Fig. 2(a).

[27]Our relativistic KKR Au band structure in Fig. 2(c) is in good accord with the band structure of Christensen (Ref. 28). Also, our interpretation of Au(100) features $A-D$ is similar to that of Ref. 17.

[28]N. E. Christensen and B. O. Seraphin, Phys. Rev. B **4**, 3321 (1971).

[29]As seen from Fig. 3 of Ref. 17, the Au(100) features of $A-F$ are of bulk origin because they can be identified on the Au(100)-(1×1) surface as well as the reconstructed Au(100)-(5×20) surface. The uppermost Δ_6 band must not give a distinct spectral feature because of levels of Δ_6 symmetry generally yield small peaks (e.g., C or E) in Au(100), and as seen from Fig. 2(c), emission from the uppermost Δ_6 level is likely to be masked by closely placed more intense emissions (A and B) from the two Δ_7 bands which sandwich this Δ_6 level; the peak B may however contain contribution from the Δ_6 level. Finally, as Fig. 2(c) shows, F does not correlate well with any of the Au(100) levels. F may be a density of states effect associated with the level Γ_{7^+}; this feature is not discernible in the alloy spectra and is not discussed further.

[30]J. Hermanson, Solid State Commun. **22**, 9 (1977). Nonrelativistic selection rules derived in this reference alloy normal emission from the (100) surface only from the d-like Δ_5 and as s-p-like Δ_1 bands. In the relativistic theory, as a result of the spin-orbit interaction, all bands (Δ_7 and Δ_6 symmetries) contribute to photoemission.

[31]A. Bansil, Phys. Rev. Lett. **41**, 1670 (1978).

[32]R. S. Rao, A. Bansil, H. Asonen, and M. Pessa, Phys. Rev. B **29**, 1713 (1984).

[33]S. Hüfner, G. K. Wertheim, and J.H. Wernick, Solid State Commun. **17**, 1585 (1975).

[34]B. Ginatempo and J. B. Staunton, J. Phys. F **18**, 1827 (1988).

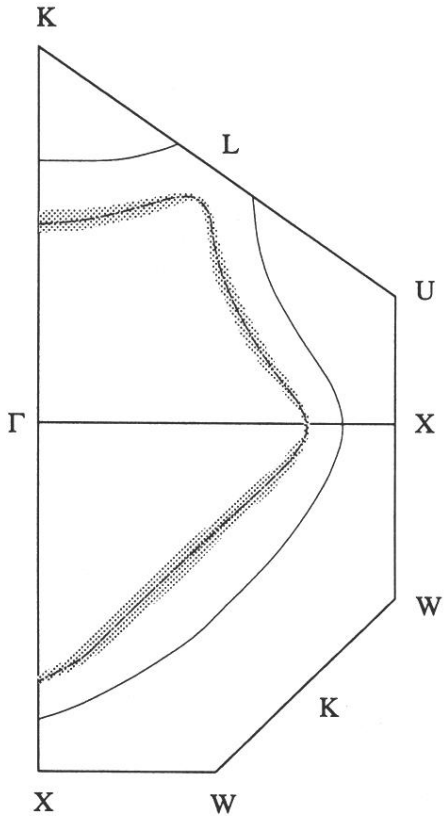

FIG. 5. The Fermi surface cross section in Γ*XWK* and Γ*XULK* planes in Au (solid) and $Au_{70}Pd_{30}$ (shaded). The shading on the alloy curve represents the disorder smearing of the Fermi surface.